Effects of temporal modeling on the statistical uncertainty of spatiotemporal distributions estimated directly from dynamic SPECT projections

B W Reutter†, G T Gullberg‡ and R H Huesman†

† Center for Functional Imaging, Lawrence Berkeley National Laboratory, University of California, Berkeley, CA 94720, USA
‡ Medical Imaging Research Laboratory, Department of Radiology, University of Utah, Salt Lake City, UT 84108, USA

E-mail: `bwreutter@lbl.gov`, `ggullbe@hsc.utah.edu`, `rhhuesman@lbl.gov`

Abstract. Artifacts can result when reconstructing a dynamic image sequence from inconsistent single photon emission computed tomography (SPECT) projection data acquired by a slowly rotating gantry. The artifacts can lead to biases in kinetic parameters estimated from time-activity curves generated by overlaying volumes of interest on the images. Insufficient sampling and truncation of projections by cone-beam collimators can cause additional artifacts. To overcome these sources of bias in conventional image based dynamic data analysis, we have been investigating the estimation of time-activity curves and kinetic model parameters directly from dynamic SPECT projection data by modeling the spatial and temporal distribution of the radiopharmaceutical throughout the projected field of view. In the present work, we perform Monte Carlo simulations to study the effects of the temporal modeling on the statistical variability of the reconstructed spatiotemporal distributions. The simulations utilize fast methods for fully four-dimensional (4-D) direct estimation of spatiotemporal distributions and their statistical uncertainties, using a spatial segmentation and temporal B-splines. The simulation results suggest that there is benefit in modeling higher orders of temporal spline continuity. In addition, the accuracy of the time modeling can be increased substantially without unduly increasing the statistical uncertainty, by using relatively fine initial time sampling to capture rapidly changing activity distributions.

1. Introduction

Artifacts can result when reconstructing a dynamic image sequence from inconsistent single photon emission computed tomography (SPECT) projection data acquired by a slowly rotating gantry. The artifacts can lead to biases in kinetic parameters estimated from time-activity curves generated by overlaying volumes of interest on the images. Insufficient sampling and truncation of projections by cone-beam collimators can cause additional artifacts (Tuy 1983). To overcome these sources of bias in conventional image based dynamic data analysis, we and others have been investigating the estimation of time-activity curves and kinetic model parameters directly from dynamic SPECT projection data by modeling the spatial and temporal distribution of the radiopharmaceutical throughout the projected field of view (Huesman *et al* 1998, Gullberg *et al* 1999, Sitek *et al* 1999, Reutter *et al* 2000, Farncombe *et al* 2001, Kadrmas and Gullberg 2001, Maltz 2001).

In our previous work we developed a fast method for fully four-dimensional (4-D) direct estimation of spatiotemporal distributions from dynamic SPECT projection data (Reutter *et al* 2000), which extended Formiconi's least-squares algorithm for reconstructing temporally static distributions (Formiconi 1993). This method can be applied to projection data acquired using any collimator or orbit geometry, provided that the data yield a preliminary image reconstruction that can be used to segment the activity distribution within the projected field of view. In addition, we studied the biases that result from modeling various orders of temporal continuity and using various time samplings (Reutter *et al* 2000). In the present work, the first goal is to address computational issues associated with evaluating the statistical uncertainty of the spatiotemporal model parameter estimates. Monte Carlo simulations are used to validate a fast algorithm for computing the covariance matrix for the parameters. Using this fast algorithm, the second goal is to complete the work begun in (Reutter *et al* 2000) by studying the statistical variability that results from modeling various orders of temporal continuity and using various time samplings.

As discussed in (Reutter *et al* 2000), these fast methods are essential for performing more detailed spatiotemporal modeling using currently available computers. These methods are also essential for solving quickly a large linear least-squares subproblem embedded in a nonlinear compartmental model estimation problem in which kinetic parameters are estimated directly from projection data (Huesman *et al* 1998).

2. Fast Computation of Statistical Uncertainty for Spatiotemporal Distributions

Following our development in (Reutter *et al* 2000), time-varying activity concentrations within volumes of interest encompassing the projected SPECT field of view can be modeled by selecting a set of temporal basis functions capable of representing typical time variations and having desired smoothness properties. Similarly, the spatially

nonuniform activity concentration within a particular volume of interest can be modeled by selecting an appropriate set of spatial basis functions. Given a set of temporal basis functions and sets of spatial basis functions for the volumes of interest, coefficients for the resulting spatiotemporal basis functions can be estimated directly from the SPECT projection data, along with the covariance matrix for the coefficients.

2.1. Covariance Matrix for the Spatiotemporal Basis Function Coefficients

Denoting the projection of the mth spatial basis function along ray i at time t by $U_i^m(t)$, and the value of the nth temporal basis function at time t by $V^n(t)$, the detected count rate along ray i at time t can be modeled as

$$P_i(t) = \sum_{m=1}^{M} \sum_{n=1}^{N} a_{mn} U_i^m(t) V^n(t), \tag{1}$$

where the a_{mn} are linear coefficients, M is the number of spatial basis functions, and N is the number of temporal basis functions. Integrating equation (1) over L contiguous time intervals spanning the data acquisition from time $t_0 = 0$ to time $t_L = T$, the projection data can be modeled as

$$p_{il} = \int_{t_{l-1}}^{t_l} P_i(\tau) d\tau = \sum_{m=1}^{M} \sum_{n=1}^{N} a_{mn} \int_{t_{l-1}}^{t_l} U_i^m(\tau) V^n(\tau) d\tau. \tag{2}$$

If the time intervals are short enough so that each spatial basis projection function $U_i^m(t)$ is approximated well by a piecewise constant function with amplitude u_{il}^m during time interval $[t_{l-1}, t_l]$, then the model for the projection data can be simplified:

$$p_{il} = \sum_{m=1}^{M} \sum_{n=1}^{N} a_{mn} u_{il}^m v_l^n, \tag{3}$$

where v_l^n is the integral $\int_{t_{l-1}}^{t_l} V^n(\tau) d\tau$ of the nth temporal basis function.

In this work we consider a periodic detector trajectory composed of K periods with J time intervals per period (i.e., K circular rotations with J angles per rotation). Replacing the time index $l = 1, ..., L$ with the indices $\{jk; j = 1, ..., J; k = 1, ..., K\}$ and dropping the index k from the now-periodic spatial basis projection factors, the projection equations (3) can be expressed as

$$p_{ijk} = \sum_{m=1}^{M} \sum_{n=1}^{N} a_{mn} u_{ij}^m v_{jk}^n. \tag{4}$$

The criterion which is minimized by varying the linear coefficients a_{mn} is the weighted sum of squares function

$$\chi^2 = \sum_{i=1}^{I} \sum_{j=1}^{J} \sum_{k=1}^{K} \frac{(p_{ijk}^* - p_{ijk})^2}{W_{ijk}}, \tag{5}$$

where the p_{ijk}^* are the measured projections, the W_{ijk} are weighting factors, and I is the number of projection rays acquired simultaneously by the detector. Typically, the weighting factors are either unity for an unweighted fit or the estimated variances of the projections for a weighted fit.

Equations (4) and (5) can be rewritten in matrix form as

$$\mathbf{p} = \mathbf{Fa} \tag{6}$$

and

$$\chi^2 = (\mathbf{p}^* - \mathbf{Fa})^{\mathrm{T}}\boldsymbol{\Phi}^{-1}(\mathbf{p}^* - \mathbf{Fa}), \tag{7}$$

respectively, where $\mathbf{p}$ is an IJK element column vector whose $[i+(j-1)I+(k-1)IJ]^{\mathrm{th}}$ element is p_{ijk}, $\mathbf{F}$ is an $IJK \times MN$ matrix whose $\{[i+(j-1)I+(k-1)IJ],[m+(n-1)M]\}^{\mathrm{th}}$ element is $u_{ij}^m v_{jk}^n$, $\mathbf{a}$ is an MN element column vector whose $[m+(n-1)M]^{\mathrm{th}}$ element is a_{mn}, $\mathbf{p}^*$ is an IJK element column vector whose $[i+(j-1)I+(k-1)IJ]^{\mathrm{th}}$ element is p_{ijk}^*, and $\boldsymbol{\Phi}^{-1}$ is an $IJK \times IJK$ diagonal matrix whose $[i+(j-1)I+(k-1)IJ]^{\mathrm{th}}$ diagonal element is $1/W_{ijk}$. The criterion, χ^2, is minimized by the vector of spatiotemporal basis function coefficients

$$\hat{\mathbf{a}} = (\mathbf{F}^{\mathrm{T}}\boldsymbol{\Phi}^{-1}\mathbf{F})^{-1}\mathbf{F}^{\mathrm{T}}\boldsymbol{\Phi}^{-1}\mathbf{p}^*. \tag{8}$$

The covariance matrix for this weighted least-squares estimate $\hat{\mathbf{a}}$ is

$$\mathrm{cov}(\hat{\mathbf{a}}) = (\mathbf{F}^{\mathrm{T}}\boldsymbol{\Phi}^{-1}\mathbf{F})^{-1}\mathbf{F}^{\mathrm{T}}\boldsymbol{\Phi}^{-1}\mathrm{cov}(\mathbf{p}^*)\boldsymbol{\Phi}^{-1}\mathbf{F}(\mathbf{F}^{\mathrm{T}}\boldsymbol{\Phi}^{-1}\mathbf{F})^{-1}, \tag{9}$$

where $\mathrm{cov}(\mathbf{p}^*)$ is the covariance matrix for the measured projections.

Given an estimate of $\mathrm{cov}(\mathbf{p}^*)$, estimates of the statistical uncertainties of the coefficients $\hat{\mathbf{a}}$ are the square roots of the diagonal elements of the covariance matrix given by equation (9) and are denoted individually by $\hat{\sigma}_{\hat{a}_{mn}}$. In general, the errors in the coefficients are correlated and the covariance matrix given by equation (9) has nonzero elements off the diagonal. Thus, to understand fully the nature of statistical fluctuations of spline models for time-activity curves, an estimate of the entire covariance matrix is needed. The full covariance information is used in section 2.2 to define a figure of merit related to the global precision of spline models.

For computational speed, $\boldsymbol{\Phi}^{-1}$ can be set to the identity matrix and an unweighted least-squares reconstruction of the coefficients $\hat{\mathbf{a}}$ can be performed. An estimate of the symmetric $MN \times MN$ covariance matrix $\mathrm{cov}(\hat{\mathbf{a}})$ can then be obtained quickly from equation (9) as follows. Assuming Poisson noise, the diagonal matrix having the modeled projections $\hat{\mathbf{p}} = \mathbf{F}\hat{\mathbf{a}}$ along the diagonal can be used as an estimate of the covariance matrix for the measured projections. Substituting this diagonal matrix for $\mathrm{cov}(\mathbf{p}^*)$ and the identity matrix for $\boldsymbol{\Phi}^{-1}$, equation (9) can be rewritten as

$$\mathrm{cov}(\hat{\mathbf{a}}) = (\mathbf{F}^{\mathrm{T}}\mathbf{F})^{-1}\mathbf{F}^{\mathrm{T}}\mathrm{diag}(\mathbf{F}\hat{\mathbf{a}})\mathbf{F}(\mathbf{F}^{\mathrm{T}}\mathbf{F})^{-1}. \tag{10}$$

We have presented a method for quickly calculating $(\mathbf{F}^{\mathrm{T}}\mathbf{F})^{-1}$ in (Reutter *et al* 2000). Using a similar development, the symmetric $MN \times MN$ matrix $\mathbf{F}^{\mathrm{T}}\mathrm{diag}(\mathbf{F}\hat{\mathbf{a}})\mathbf{F}$ can be calculated quickly as follows. Denoting the $\{[m+(n-1)M],[m'+(n'-1)M]\}^{\mathrm{th}}$ element of $\mathbf{F}^{\mathrm{T}}\mathrm{diag}(\mathbf{F}\hat{\mathbf{a}})\mathbf{F}$ by $\psi^{mnm'n'}$, one has

$$\psi^{mnm'n'} = \sum_{i=1}^{I}\sum_{j=1}^{J}\sum_{k=1}^{K} u_{ij}^m v_{jk}^n \left[\sum_{m''=1}^{M}\sum_{n''=1}^{N} \hat{a}_{m''n''} u_{ij}^{m''} v_{jk}^{n''}\right] u_{ij}^{m'} v_{jk}^{n'}, \tag{11}$$

where $\hat{a}_{m''n''}$ is the $[m'' + (n'' - 1)M]^{\text{th}}$ element of $\hat{\mathbf{a}}$. Rearranging the summations yields

$$
\begin{aligned}
\psi^{mnm'n'} &= \sum_{m''=1}^{M} \sum_{n''=1}^{N} \hat{a}_{m''n''} \sum_{j=1}^{J} \left[\sum_{i=1}^{I} u_{ij}^{m} u_{ij}^{m'} u_{ij}^{m''} \right] \left[\sum_{k=1}^{K} v_{jk}^{n} v_{jk}^{n'} v_{jk}^{n''} \right] \\
&= \sum_{m''=1}^{M} \sum_{n''=1}^{N} \hat{a}_{m''n''} \sum_{j=1}^{J} \alpha_{j}^{mm'm''} \beta_{j}^{nn'n''} \\
&= \sum_{m''=1}^{M} \sum_{n''=1}^{N} \hat{a}_{m''n''} \gamma^{mnm'n'm''n''},
\end{aligned}
\tag{12}
$$

where the factors $\alpha_{j}^{mm'm''}$ and $\beta_{j}^{nn'n''}$ denote the summations $\sum_{i=1}^{I} u_{ij}^{m} u_{ij}^{m'} u_{ij}^{m''}$ and $\sum_{k=1}^{K} v_{jk}^{n} v_{jk}^{n'} v_{jk}^{n''}$, respectively, and the factor $\gamma^{mnm'n'm''n''}$ denotes the sum $\sum_{j=1}^{J} \alpha_{j}^{mm'm''} \beta_{j}^{nn'n''}$.

Using the factorization given by equation (12), it can be shown that most of the overhead associated with computing the symmetric matrix elements $\psi^{mnm'n'}$ lies in calculating the $\alpha_{j}^{mm'm''}$ factors and the $\gamma^{mnm'n'm''n''}$ factors. These calculations take about $[(I/N^3) + 1]JMNQ$ multiply-and-add operations, where $Q = (MN)(MN + 1)/2$. By comparison, relatively straightforward computation of the summations given by equation (11) takes about $IJKQ$ multiply-and-add operations. Thus, for the simulated dynamic cardiac cone-beam SPECT studies described in section 3, for which $I/N^3 = 1/2$, the factorization given by equation (12) reduces the computation by a factor of about $2IK/3MN \approx 200$.

2.2. Covariance Between Integrated Time-Activity Curve Model Segments

Given an estimate of the covariance matrix, $\text{cov}(\hat{\mathbf{a}})$, for the spatiotemporal basis function coefficients, estimates of the covariance between integrated segments of the time-activity curve models for the volumes of interest can be obtained as follows.

The integral of the time-activity curve model for volume of interest m, during the time interval associated with angle j of rotation k, can be expressed as $\sum_{n=1}^{N} \hat{a}_{mn} v_{jk}^{n}$. Thus, the covariance of this time integral with the time integral associated with volume of interest m' during angle j' of rotation k' is

$$
\text{cov}\left(\sum_{n=1}^{N} \hat{a}_{mn} v_{jk}^{n}, \sum_{n=1}^{N} \hat{a}_{m'n} v_{j'k'}^{n} \right) = \sum_{n=1}^{N} \sum_{n'=1}^{N} v_{jk}^{n} \text{cov}(\hat{a}_{mn}, \hat{a}_{m'n'}) v_{j'k'}^{n'},
\tag{13}
$$

and the variance of each time integral is

$$
\sigma_{jkm}^{2} = \sum_{n=1}^{N} \sum_{n'=1}^{N} v_{jk}^{n} \text{cov}(\hat{a}_{mn}, \hat{a}_{mn'}) v_{jk}^{n'}.
\tag{14}
$$

As a figure of merit related to the global precision of the time-activity curve model for volume of interest m, the following expression yields a squared noise-to-signal ratio (NSR) calculated as the mean (over all of the time segments) of the expected values of the squared errors between the integrated segments of the "true" and modeled curves,

normalized by the mean square value of the integrated segments of the "true" curve:

$$\xi_m^2 = \frac{\sum_{j=1}^{J}\sum_{k=1}^{K}\sigma_{jkm}^2}{\sum_{j=1}^{J}\sum_{k=1}^{K}\left[\sum_{n=1}^{N}\hat{a}_{mn}v_{jk}^n\right]^2}. \tag{15}$$

Substituting equation (14) into equation (15), the squared NSR, ξ_m^2, can be calculated quickly by rearranging the summations, precomputing the inner products of the temporal basis functions, $\nu^{nn'} = \sum_{j=1}^{J}\sum_{k=1}^{K}v_{jk}^n v_{jk}^{n'}$, and exploiting the symmetry with respect to the indices n and n':

$$\xi_m^2 = \frac{\sum_{n=1}^{N}\sum_{n'=1}^{N}\mathrm{cov}(\hat{a}_{mn}, \hat{a}_{mn'})\nu^{nn'}}{\sum_{n=1}^{N}\sum_{n'=1}^{N}\hat{a}_{mn}\hat{a}_{mn'}\nu^{nn'}}. \tag{16}$$

The global NSR, ξ_m, is used in section 3 to assess the precision of temporal modeling for simulated dynamic cardiac cone-beam SPECT studies. The global NSR is also used to assess the increase in precision that would be yielded by a weighted least-squares fit that uses the covariance matrix for the projections as the weighting matrix $\mathbf{\Phi}$ in equations (7)–(9). This measure is calculated by replacing $\mathbf{p}^*$ in equation (8) with the expected values of the projections and replacing $\mathbf{\Phi}$ in equations (8) and (9) with $\mathrm{cov}(\mathbf{p}^*)$. The resulting values for $\hat{\mathbf{a}}$ and $\mathrm{cov}(\hat{\mathbf{a}})$ are then substituted into equation (16).

3. Computer Simulations

Using the simulation apparatus described in (Reutter *et al* 2000), Monte Carlo simulations were performed to validate the fast algorithm presented in section 2 and to study the effects of the temporal modeling on the statistical variability of the reconstructed spatiotemporal distributions.

Simulated spatiotemporal distributions were obtained using the Mathematical Cardiac Torso (MCAT) phantom developed at the University of North Carolina (Tsui *et al* 1993). The emission phantom (figure 1) was composed of 128 contiguous 1.75 mm-thick slices and contained the blood pool, three myocardial tissue volumes of interest (normal myocardium, septal defect, and lateral defect), liver, and background tissue. Projections were attenuated using the corresponding MCAT attenuation phantom.

The simulated time-activity curves (figure 2) mimicked the kinetics of teboroxime (Narra *et al* 1992). The simulated 15 min data acquisition consisted of $I = 2048$ cone-beam projection rays per angle (64 transverse × 32 axial), $J = 120$ angles per rotation, and $K = 15$ rotations, and thus yielded about 3.7 million projection samples. The projection bins were 7 mm × 7 mm at the detector, and the detector was 30 cm from the center of the field of view. The cone-beam collimators had a hole diameter of 2 mm, a length of 4 cm, and were offset 1 cm from the detector. The focal length was 70 cm, which resulted in truncation of the data (figure 1). Attenuation and geometric point response were modeled using a ray-driven projector with line length weighting (Zeng *et al* 1991). Scatter was not modeled. The amplitude of the simulated blood input function was adjusted so that about 10 million events were detected using the cone-beam collimators.
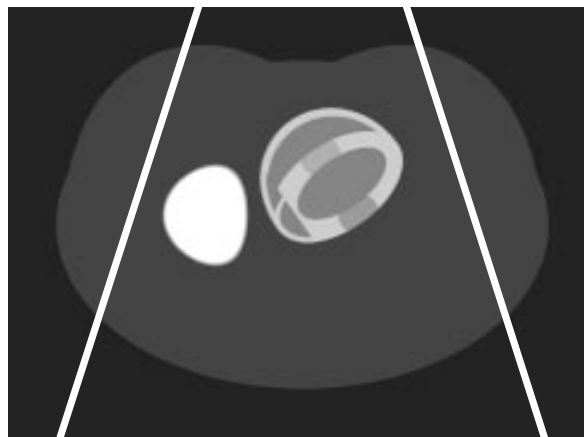
Figure 1. Transverse cross section through the MCAT emission phantom, showing the truncation of data resulting from the use of cone-beam collimators.
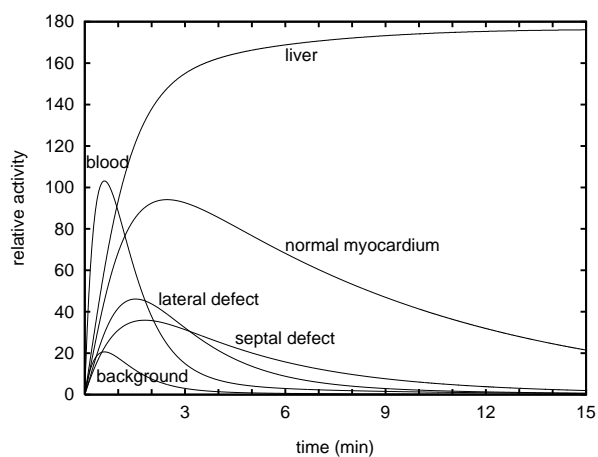

Figure 2. Simulated teboroxime time-activity curves for the volumes in figure 1.
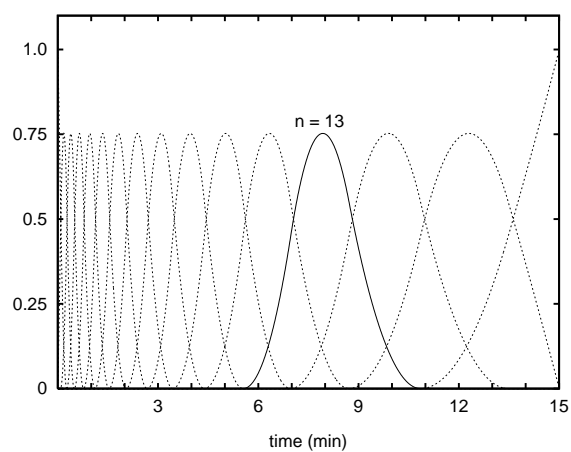

Figure 3. Sixteen piecewise quadratic B-spline temporal basis functions used to validate the fast algorithm. The thirteenth spline is shown as a solid curve.

The spatial basis projection factors u_{ij}^m were defined by forward projecting each of the six known emission volumes composing the MCAT phantom (figure 1). Each emission volume was modeled to contain spatially uniform activity, which yielded $M = 6$ sets of spatial basis projection factors.

3.1. Validation of the Fast Algorithm

A set of 1600 realizations of projection data having Poisson noise was generated and reconstructed using temporal basis integral factors v_{jk}^n that were defined by integrating $N = 16$ splines spanning 15 time segments having geometrically increasing length (figure 3). Piecewise quadratic B-splines were used with an initial time segment length of 10 sec. The resulting curve models were continuous through their first derivative. For noiseless projections, the modeling error was less than 2%, where the error was defined to be the root mean square (RMS) difference between the simulated curve and the spline model, normalized by the RMS value of the simulated curve (Reutter *et al* 2000).

The computational benefit of using the factorization given by equation (12) to estimate the covariance matrix for the spatiotemporal basis function coefficients was evident in the simulations. The number of multiply-and-add operations used to calculate $\mathbf{F}^{\mathrm{T}}\mathrm{diag}(\mathbf{F\hat{a}})\mathbf{F}$ was reduced by a factor of about 200 so that only 80 million multiply-and-adds were needed, instead of 17 billion. Using a 194-MHz R10000-based SGI workstation, it took 34 sec to estimate the 96 coefficients for the spatiotemporal basis functions, their covariance matrix, and the squared noise-to-signal ratios given by equation (16).

Table 1 shows that for the blood pool and myocardial tissue volumes, the sample means of the $\hat{\sigma}_{\hat{a}_{mn}}$ (the square roots of the diagonal elements of the estimated covariance matrix) were within 5% of the sample standard deviations of the $\hat{a}_{mn}$ (the estimated spatiotemporal basis function coefficients). For the liver and background tissue, the agreement was to within 4% (data not shown). The coefficients of variation for the $\hat{\sigma}_{\hat{a}_{mn}}$ were less than 2% (data not shown).

Table 2 shows that the sample means of the ξ_m (the estimated NSRs given by equation (16)) were within 4% of the sample means of the RMS differences between the 1600 sets of time-activity curve models and their corresponding mean curves, normalized by the RMS values of the mean curves. The curves for the septal and lateral defects exhibited the largest variability because of their small spatiotemporal support, i.e., the normal myocardium had a volume that was about 30 times greater than that of each defect (250 cc compared to 8.4 cc) and the RMS value for the activity density in the normal myocardium was about three times greater than that in the defects.

Table 2 also shows that the NSR would improve slightly when performing a weighted least-squares fit that uses the covariance matrix for the projections as the weighting matrix $\mathbf{\Phi}$ in equations (7)–(9).

Table 1. Sample means and sample standard deviations of the spatiotemporal basis function coefficients $\hat{a}_{mn}$, and sample means of the estimated coefficient uncertainties $\hat{\sigma}_{\hat{a}_{mn}}$, for 1600 realizations of noisy projections. For each volume of interest, the sample standard deviations of the coefficients $\hat{a}_{mn}$ agree closely with the sample means of the estimated uncertainties $\hat{\sigma}_{\hat{a}_{mn}}$.

	blood pool			normal myocardium			septal defect			lateral defect		
n	$\hat{a}_{1n}$		$\hat{\sigma}_{\hat{a}_{1n}}$	$\hat{a}_{2n}$		$\hat{\sigma}_{\hat{a}_{2n}}$	$\hat{a}_{3n}$		$\hat{\sigma}_{\hat{a}_{3n}}$	$\hat{a}_{4n}$		$\hat{\sigma}_{\hat{a}_{4n}}$
	mean	sdev	mean	mean	sdev	mean	mean	sdev	mean	mean	sdev	mean
1	0.279	0.128	0.131	0.0102	0.166	0.166	−0.0529	1.28	1.29	−0.212	0.747	0.762
2	5.20	0.138	0.140	1.05	0.171	0.174	0.559	1.33	1.35	0.979	1.47	1.46
3	7.65	0.157	0.160	2.30	0.185	0.187	1.36	1.89	1.88	1.38	3.00	2.99
4	8.20	0.172	0.175	3.75	0.331	0.333	1.89	3.04	3.05	2.42	1.95	1.95
5	7.19	0.153	0.160	5.15	0.222	0.219	2.33	1.91	1.94	3.25	1.26	1.27
6	5.40	0.105	0.107	6.30	0.148	0.145	2.70	1.20	1.24	3.58	1.75	1.73
7	3.51	0.0974	0.0953	7.07	0.141	0.140	2.87	1.50	1.54	3.59	0.876	0.864
8	2.00	0.0658	0.0668	7.36	0.108	0.109	2.67	0.886	0.904	3.11	1.08	1.09
9	1.04	0.0545	0.0543	7.21	0.0839	0.0836	2.45	0.600	0.602	2.44	0.593	0.602
10	0.535	0.0464	0.0446	6.71	0.0743	0.0735	2.02	0.560	0.562	1.69	0.418	0.411
11	0.308	0.0361	0.0362	5.98	0.0632	0.0628	1.57	0.486	0.477	1.03	0.364	0.354
12	0.208	0.0305	0.0298	5.13	0.0538	0.0530	1.13	0.397	0.399	0.592	0.296	0.300
13	0.149	0.0250	0.0245	4.20	0.0454	0.0441	0.761	0.327	0.325	0.307	0.258	0.253
14	0.103	0.0197	0.0201	3.28	0.0360	0.0365	0.478	0.268	0.270	0.179	0.206	0.207
15	0.0657	0.0167	0.0168	2.39	0.0303	0.0308	0.268	0.232	0.234	0.0853	0.165	0.170
16	0.0399	0.0169	0.0169	1.64	0.0314	0.0313	0.135	0.270	0.269	0.0651	0.161	0.164

Table 2. Sample means and sample standard deviations of observed and estimated noise-to-signal ratios for time-activity curves, for 1600 realizations of noisy projections. A weighted least-squares (WLS) fit would improve the NSR slightly.

	observed NSR (%)		estimated NSR ξ_m (%)		WLS ξ_m (%)
	mean	sdev	mean	sdev	
blood pool	1.51	0.35	1.56	0.008	1.47
normal myocardium	1.13	0.27	1.16	0.003	1.08
septal defect	32.5	9.1	32.5	2.6	32.4
lateral defect	28.5	8.0	28.6	2.3	28.3
liver	0.167	0.031	0.170	0.0001	0.158
background	0.242	0.058	0.247	0.0002	0.225

3.2. Effects of Temporal Modeling

To study the statistical variability that results from modeling various orders of temporal continuity and using various time samplings, 24 sets of 1000 realizations of projection data having Poisson noise were generated. Each set of 1000 projections

was reconstructed using a different set of temporal basis functions consisting of $N = 16$ splines spanning 15 time segments having geometrically increasing length (e.g., figure 3). Piecewise cubic, quadratic, linear, or constant B-splines were used with initial time segment lengths of 2.5, 5, 10, 20, 40, or 60 sec.

Figure 4 shows the results for the blood pool and three myocardial tissue volumes. For each temporal basis set and volume of interest, there was close agreement between the sample mean of the estimated NSR, ξ_m, and the observed NSR, which was calculated as described in the caption for figure 4. The effect of the polynomial order of the splines on the NSR was relatively small, while the effect of the time sampling was larger. The NSR tended to decrease as the time sampling became more uniform (e.g., for initial time segment lengths of 40 or 60 sec). However, the decrease in NSR was offset by an increase in normalized RMS bias, which was calculated as described in the caption for figure 4. The normalized RMS bias increased because these basis sets had initial samplings that were too long to accurately model the beginning of the acquisition, when the activity concentrations were changing most rapidly (figure 2). The normalized RMS bias also tended to increase as the polynomial order of the splines decreased.

The combined effects of statistical fluctuations measured by the NSR and modeling errors measured by normalized RMS bias were studied by adding the quantities in quadrature (i.e., taking the square root of the sum of their squares). The resulting total expected RMS error for the blood pool reached a minimum of 1.6% when using cubic or quadratic splines having initial time samplings of 10 sec or less. Using these same sets of temporal basis functions, the total error for the background did not exceed 0.7% (data not shown). For the myocardial volumes, the total error was at its lowest when using cubic, quadratic, or linear splines having initial time samplings of 20 sec or less. Using these basis functions, the total error for the normal myocardium, septal defect, and lateral defect ranged between 1.0–1.3%, 30–35%, and 24–33%, respectively. The total absolute RMS error for each defect was only about 10% of the RMS value of the time-activity curve for the normal myocardium. This absolute error was sufficiently small to allow the defects to be discriminated from the normal myocardium. The total error for the liver was 0.2% (data not shown).

4. Discussion

The fast algorithm presented in section 2 facilitated the study of the statistical variability that results from modeling various orders of temporal continuity and using various time samplings, when estimating spatiotemporal distributions directly from dynamic cone-beam SPECT projection data. The simulation results presented in section 3 suggest that there is benefit in modeling higher orders of temporal continuity. In addition, it appears that the accuracy of time-activity curve models can be increased substantially without unduly increasing their statistical uncertainty, by using relatively fine initial time sampling to capture rapidly changing activity distributions. A future goal is to introduce the initial time sampling of the splines as a nonlinear parameter that is
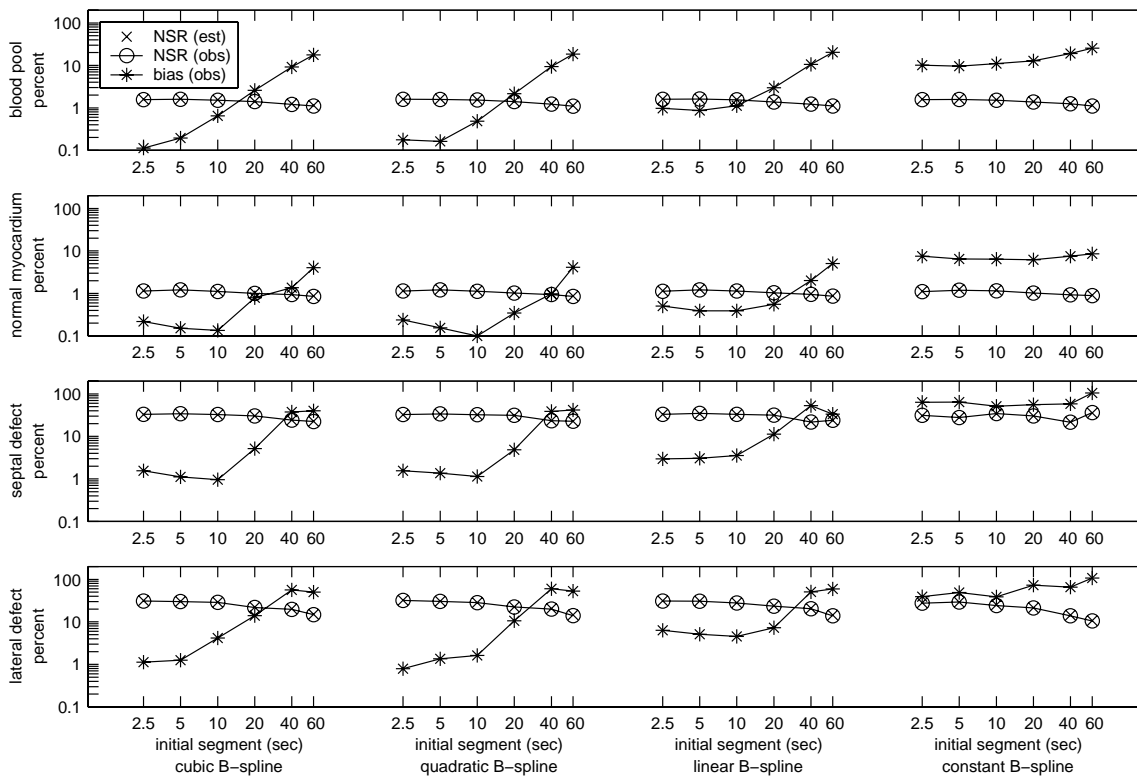
Figure 4. Effects of temporal modeling. The "∗" symbols denote normalized RMS bias values observed for 1000 realizations of noisy projections. For each temporal basis set, normalized RMS bias was calculated by first calculating the mean time-activity curve for the 1000 noisy curves, and then calculating the RMS difference between the mean noisy curve and the simulated curve (figure 2). The RMS difference was then normalized by the RMS value for the simulated curve and expressed as a percentage. The "○" symbols denote the observed NSR for each basis set, which was calculated as the mean value of the RMS differences between the 1000 noisy curves and the mean noisy curve, normalized by the RMS value of the mean noisy curve, and expressed as a percentage. The "×" symbols denote mean values of estimated NSR, ξ_m, calculated using equation (16). These values agree closely with the observed NSR values.

optimized in conjunction with the spline coefficients.

Although the estimation of compartmental model parameters from directly estimated time-activity curves was not considered here, the fast covariance calculation could help to improve kinetic data analysis. By incorporating information about the full covariance between time-activity curve models for the blood input function and tissue volumes, kinetic parameter estimates could be estimated more precisely (Huesman and Mazoyer 1987, Kadrmas *et al* 1999).

Future work also includes the joint estimation of a temporal spline model for the blood input function and kinetic parameters for compartmental models directly from the projection data. To improve the detail of spatial modeling, we plan to increase the number of segmented volumes encompassing the projected field of view and to parameterize spatially nonuniform activity concentrations within the volumes.

Acknowledgments

References

Farncombe T, Celler A, Bever C, Noll D, Maeght J and Harrop R 2001 The incorporation of organ uptake into dynamic SPECT (dSPECT) image reconstruction *IEEE Trans. Nucl. Sci.* **48** 3–9

Formiconi A R 1993 Least squares algorithm for region-of-interest evaluation in emission tomography *IEEE Trans. Med. Imaging* **12** 90–100

Gullberg G T, Huesman R H, Ross S G, Di Bella E V R, Zeng G L, Reutter B W, Christian P E and Foresti S A 1999 Dynamic cardiac single-photon emission computed tomography *Nuclear Cardiology: State of the Art and Future Directions* ed B L Zaret and G A Beller (St. Louis, Mo.: Mosby) pp 137–87

Huesman R H and Mazoyer B M 1987 Kinetic data analysis with a noisy input function *Phys. Med. Biol.* **32** 1569–79

Huesman R H, Reutter B W, Zeng G L and Gullberg G T 1998 Kinetic parameter estimation from SPECT cone-beam projection measurements *Phys. Med. Biol.* **43** 973–82

Kadrmas D J, Di Bella E V R, Huesman R H and Gullberg G T 1999 Analytical propagation of errors in dynamic SPECT: estimators, degrading factors, bias and noise *Phys. Med. Biol.* **44** 1997–2014

Kadrmas D J and Gullberg G T 2001 4D maximum *a posteriori* reconstruction in dynamic SPECT using a compartmental model-based prior *Phys. Med. Biol.* **46** 1553–74

Maltz J S 2001 Optimal time-activity basis selection for exponential spectral analysis: application to the solution of large dynamic emission tomographic reconstruction problems *IEEE Trans. Nucl. Sci.* **49** 1452–64

Narra R K, Feld T and Nunn A D 1992 Absorbed radiation dose to humans from technetium-99m-teboroxime *J. Nucl. Med.* **33** 88–93

Reutter B W, Gullberg G T and Huesman R H 2000 Direct least-squares estimation of spatiotemporal distributions from dynamic SPECT projections using a spatial segmentation and temporal B-splines *IEEE Trans. Med. Imaging* **19** 434–50

Sitek A, Di Bella E V R and Gullberg G T 1999 Reconstruction from slow rotation dynamic SPECT using a factor model *Information Processing in Medical Imaging: 16th Int. Conf., IPMI'99 (Visegrád)* ed A Kuba *et al* (Berlin: Springer) pp 436–41

Tsui B M W, Terry J A and Gullberg G T 1993 Evaluation of cardiac cone-beam single photon emission computed tomography using observer performance experiments and receiver operating characteristic analysis *Inv. Radiol.* **28** 1101–12

Tuy H K 1983 An inversion formula for cone-beam reconstruction *SIAM J. Appl. Math.* **43** 546-52

Zeng G L, Gullberg G T, Tsui B M W and Terry J A 1991 Three-dimensional iterative reconstruction algorithms with attenuation and geometric point response correction *IEEE Trans. Nucl. Sci.* **38** 693–702

Disclaimer